Effect of the valence state on the band magnetocrystalline anisotropy in two-dimensional rare-earth/noble-metal compounds

M. Blanco-Rey [1,2] R. Castrillo-Bodero,[3] K. Ali,[2,3] P. Gargiani,[4] F. Bertran [5] P. M. Sheverdyaeva [6] J. E. Ortega,[7,3,2] L. Fernandez [7,3] and F. Schiller [3,2]

[1]*Departamento de Polímeros y Materiales Avanzados: Física, Química y Tecnología, Universidad del País Vasco UPV-EHU, 20018 San Sebastián, Spain*

[2]*Donostia International Physics Center, 20018 Donostia-San Sebastián, Spain*

[3]*Centro de Física de Materiales CSIC/UPV-EHU-Materials Physics Center, 20018 San Sebastián, Spain*

[4]*ALBA Syncharotron Light Source, Carretera BP 1413 km 3.3, 08290 Cerdanyola del Vallès, Spain*

[5]*Synchrotron SOLEIL, CNRS-CEA, L'Orme des Merisiers Saint-Aubin, Boîte Postale 48, 91192 Gif-sur-Yvette, France*

[6]*Instituto di Struttura della Materia, Consiglio Nazionale delle Ricerche, 34149 Trieste, Italy*

[7]*Departamento de Física Aplicada I, Universidad del País Vasco UPV/EHU, 20018 San Sebastián, Spain*

In intermetallic compounds with zero orbital momentum ($L = 0$) the magnetic anisotropy and the electronic band structure are interconnected. Here, we investigate this connection in divalent Eu and trivalent Gd intermetallic compounds. We find by x-ray magnetic circular dichroism an out-of-plane easy magnetization axis in two-dimensional atom-thick $EuAu_2$. Angle-resolved photoemission spectroscopy and density-functional theory prove that this is due to strong f-d band hybridization and Eu^{2+} valence. In contrast, the easy in-plane magnetization of the structurally equivalent $GdAu_2$ is ruled by spin-orbit-split d bands, notably Weyl nodal lines, occupied in the Gd^{3+} state. Regardless of the L value, we predict a similar itinerant electron contribution to the anisotropy of analogous compounds.

I. INTRODUCTION

Spin-orbit coupling (SOC) is responsible for the splitting of a $4f^n$ orbital into multiplet states $|JJ_z\rangle$ defined by the total angular momentum J and its projection J_z on the magnetization direction. If these levels are accessible by the crystal field energies, quenching of $\langle J_z \rangle$ can occur. The orientation dependence of this mixing of states is at the origin of the strong magnetocrystalline anisotropy of systems based on rare earth (RE) elements [1,2]. In recent years, magnets in the zero-dimensional limit have been successfully realized using REs, either as isolated adatoms [3–7] or as centers in organic molecules [8–14]. Prior to these achievements it was known that the $4f$ electron shell confers to bulk intermetallic RE compounds uniaxial anisotropy and high Curie temperatures T_C (and consequently large coercive fields) [15], where the magnetic coupling follows a Ruderman-Kittel-Kasuya-Yosida mechanism [16]. In two-dimensional (2D) rare-earth/noble-metal (RE/NM) surface compounds large T_C values are retained [17–22]. Anisotropy is a requisite for stable long-range magnetic ordering in two dimensions [23–25]. Magneto-optic Kerr effect and x-ray

magnetic circular dichroism (XMCD) studies have revealed that the magnetocrystalline anisotropy in these compounds does not follow a common trend. For example, the $HoAu_2$ monolayer (ML) grown on Au(111) is strongly anisotropic with an out-of-plane (OOP) easy axis, whereas the $GdAu_2$ one is more easily magnetized in plane (IP). The $HoAu_2$ case can be understood in terms of the $^5H_8$ state given by Hund's rule for $4f^{10}$ (Ho^{3+}) since the oblate shape of the orbital and the surface charge distribution favor an OOP easy axis [9,22]. However, explaining the $GdAu_2$ anisotropy demands an extension of the model. In fact, the $4f$ shell of Gd^{3+} is half filled; that is, the total orbital quantum number is $L = 0$ ($^8S_{7/2}$ ground state), and the hybridization with the surface bands is negligible, and therefore, the anisotropy must have a different origin.

At half filling $4f^7$, classical dipolar interactions tend to dominate the anisotropy in bulk Gd compounds [26,27], yet the magnetocrystalline contribution is not fully quenched, as observed in metallic hcp Gd [28]. The latter results from the spin polarization of the $5d$ conduction electrons, which are also subject to SOC [29,30]. This leads to sizable magnetocrystalline anisotropy energy (MAE) values and nonzero orbital momenta [31].

In this work, we show that the magnetocrystalline anisotropy of R-M_2 MLs (where R = rare earth and M = noble metal) is not defined only by the $4f$ single-orbital anisotropy and there exists an additional term originating at the itinerant electrons. Since all the compounds of the R-M_2 family display similar band dispersion features, the

calculations presented here for $L = 0$ systems, namely, EuAu$_2$ and GdAu$_2$, predict that the itinerant electrons contribute to the MAE with ≈ 1 meV in general and that the RE valence state determines whether this contribution favors an OOP or IP easy axis of magnetization. This means that, for RE materials with a large $4f$ single-orbital anisotropy, the total anisotropy will not depend on the band dispersion. For other RE metals, however, the band dispersion may define the magnetic anisotropy. We show that Eu in the EuAu$_2$ ML on Au(111) behaves as a divalent species and thus it is nominally in an $^8S_{7/2}$ ground state, like Gd^{3+} in the GdAu$_2$ ML. However, an EuAu$_2$ ML presents an OOP easy axis of magnetization and MAE $= 1.6$ meV, in contrast to the IP easy axis observed in GdAu$_2$. The IP easy axis of GdAu$_2$ is explained in terms of the SOC lifting degeneracies in dispersive valence bands with Gd(d) character. On the other hand, in divalent EuAu$_2$ the Eu(d) states are unoccupied and do not contribute. Instead, the anisotropy is caused by the strong f-d band hybridization.

II. METHODS

A. Experimental methods

Sample preparation of EuAu$_2$ was carried out by thermal deposition of Eu onto a clean Au(111) single-crystalline surface. The formation of the monolayer is achieved when a complete layer with moiré is observed by scanning tunneling microscopy (STM), or the surface state emission of the Au(111) Shockley state in angle-resolved photoemission spectroscopy (ARPES) [32,33] has completely vanished. The substrate temperature is around 675 K for GdAu$_2$, whereas for EuAu$_2$ a precise temperature of 575 K is required. The prepared EuAu$_2$ and GdAu$_2$ ML systems reveal a $\sqrt{3} \times \sqrt{3}$R30° atomic arrangement and a long range order moiré lattice with respect to the underlaying Au(111) substrate. This superstructure is easily distinguishable in low-energy electron diffraction (LEED) images and serves as a quality indicator in XMCD synchrotron preparations.

The EuAu$_2$ XMCD measurements were performed at the Boreas beamline of the Spanish synchrotron radiation facility ALBA using a 90% circularly polarized light from a helical undulator. The measurements were undertaken at 2–20 K with a variable magnetic field up to ± 6 T. The applied magnetic field $\vec{H}$ was aligned with the photon propagation vector. The XMCD spectrum is the difference between the two x-ray absorption spectroscopy (XAS) spectra recorded with opposite orientation of the magnetic field and/or the circular helicity of the light, which we call μ_+ and μ_- for simplicity. The XMCD signal is proportional to the projection of the magnetization in the direction of the applied magnetic field. At normal light incidence, the field is also normal to the sample surface (out-of-plane geometry), while at grazing incidence (here 70°), the magnetic field is nearly parallel to the surface (in-plane geometry). The magnetization curves are taken by varying continuously the applied field with the sample kept in one of the mentioned geometries for both circular helicities. For normalization issues, at each field value two XAS absorption values were taken, the first one corresponding to the photon energy of the maximum of the XMCD signal and the second one at a slightly lower photon energy prior to the XAS
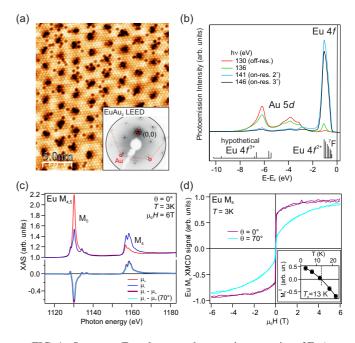
FIG. 1. Structure, Eu valence, and magnetic properties of EuAu$_2$. (a) STM image ($U = -2$ V, $I = 200$ pA). Inset: LEED pattern at $E = 40$ eV energy; the red circles mark the Au(111) substrate spots prior to EuAu$_2$ formation. (b) Resonant photoemission across the $4d \rightarrow 4f$ absorption edge determining the pure monolayer formation of divalent Eu atoms. The final state multiplets are taken from [50,51]. (c) X-ray absorption at the Eu $M_{4,5}$ edge with left (μ_-) and right (μ_+) circularly polarized light at an applied field of $\mu_0H = 6$T and at $T = 3$ K in normal incidence geometry ($\theta = 0$). The difference spectrum (XMCD) is shown for normal and grazing ($\theta = 70°$) incidences. (d) Magnetization curves taken at the Eu M_5 edge in these two geometries; the inset shows the corresponding Arrott plot analysis to determine T_C.

absorption edge. In order to determine the Curie temperature T_C of the material such magnetization curves were taken for several temperatures below and above T_C.

ARPES experiments were performed at the CASSIOPEE beamline of the SOLEIL synchrotron, France, and at our home laboratory in San Sebastián (Spain) together with the STM and LEED analysis. Photoemission data at San Sebastián were acquired using He I α ($h\nu = 21.2$ eV) light. In San Sebastián and at SOLEIL a channel-plate-based display-type hemispherical analyzer was used (Specs 150 and Scienta R4000 electron analyzers) with angular and energy resolutions set to 0.1° and 40 meV, respectively. At the synchrotron, p-polarized light was used, and the sample temperature during measurements was 70 K, while sample temperature during He I α ARPES measurements was 120 K. Resonant photoemission spectroscopy (ResPES) was achieved at the Eu $4d \rightarrow 4f$ absorption edge. In such measurements the photoemission signal is resonantly enhanced due to superposition/interference of the direct photoemission process and an Auger decay and leads to a broad resonant maximum above the $4d$ absorption threshold accompanied by a number of narrow peaks caused by several decay processes that were initially explained for the $4f^7$ configuration of Gd [34] and later for the same configuration of Eu [35]. In mixed-valence Eu compounds slightly
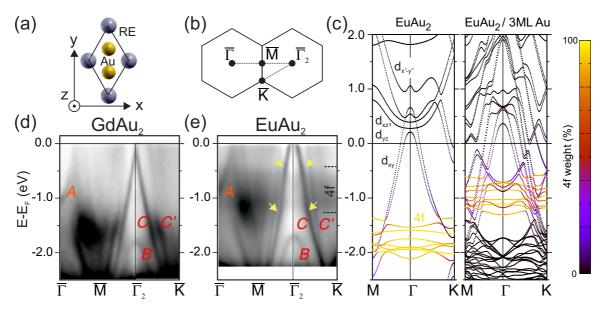
FIG. 2. Band structures of GdAu$_2$ and EuAu$_2$. (a) Model of the RAu$_2$ ML unit cell. (b) Path in the reciprocal space of the band structures measured by ARPES at photon energy $h\nu = 21.2$ eV for (d) GdAu$_2$ and (e) EuAu$_2$. (c) Band structure from DFT calculations along the indicated high-symmetry direction for a EuAu$_2$ monolayer, both freestanding (left) and on a 3 ML Au(111) slab (right). The Eu 4f contribution to the states is indicated by a color scale.

different resonant energies [36] can be used to differentiate the di- and trivalent contributions. Here, we used $h\nu = 141$ and 146 eV, corresponding to two close photon energies, in order to minimize photoemission cross-section changes but still resonantly enhance di- or trivalent signals. The off-resonant energy $h\nu = 130$ eV corresponds to a simple $(4f^7)^8S_{7/2} \rightarrow (4f^7)^7F_J$ photoemission transition. The individual J components cannot be resolved easily at such high photon energies due to worse energy resolution but have been observed for pure Eu metal at low photon energies [37].

B. Theoretical methods

Density-functional theory (DFT) calculations were performed in the full-potential linearized augmented plane wave (FLAPW) formalism [38–40] at the generalized gradient approximation $+ U$ level to describe strong correlation [41,42] in the fully localized limit method since the Eu(4f) orbital is half filled [43]. The Perdew-Burke-Ernzerhof exchange and correlation functional [44] was used. The parameter $U = 5.5$ eV is found to match the 4f bands binding energies observed in ARPES. In the case of the calculation parameters for GdAu$_2$, we refer the reader to previous work in Ref. [21], where $U = 7.5$ eV was employed. The lattice constant of the model geometries was fixed to the EuAu$_2$ experimental value. For the supported models a $\sqrt{3} \times \sqrt{3}$R30° supercell geometry was used with fcc stacking of atomic planes and an interlayer distance of 2.25 Å between the flat EuAu$_2$ monolayer and the Au(111) substrate. For the local FLAPW basis, as in previous works with RAu$_2$, R 6s, 4f, and 5d and Au 6s and 5d electrons were included as valence electrons, and R 5s and 5p and Au 5p electrons were included as linear orbitals. Partial wave expansions up to $l_{\max} = 8$ and 10 were set inside the Eu and Au muffin-tin spheres with radii of 1.43 and 1.48 Å, respectively.

SOC was included in the calculation both self-consistently and in the force theorem perturbative approximation [45–48], i.e., without carrying out further self-consistent optimization of the charge density, for spins oriented in plane (X) and out of plane (Z) [see Fig. 2(a)]. Using the force theorem, the MAE is computed as the energy difference between the band energies; that is, it is a rigid electron density approximation. The working principles of the method are described in Sec. III E. The MAE accuracy is highly dependent on the fine details of the band structure, especially the gap openings at band crossings and the Fermi level. Therefore, a fine sampling of the first Brillouin zone (BZ) and the sharpest possible Fermi-Dirac function are required. In this work, the MAE was converged with a tolerance of ~0.1 meV using a smearing width $\sigma = 5$ meV for the Fermi level (first-order Methfessel-Paxton method [49]) and a mesh of at least 25×25 k points, with plane wave expansion cutoffs of 4 and 12 bohr^{-1} for the wave functions and potential, respectively.

III. RESULTS AND DISCUSSION

A. Structure characterization

The EuAu$_2$ ML is characterized by a hexagonal moiré superstructure visible in the STM micrograph and the LEED pattern in Fig. 1(a). Similar moiré superstructures are found in other RE/NM metal surfaces [18,21,22,52]. The STM analysis of EuAu$_2$ yields a moiré superlattice constant of $a_m = (3.3 \pm 0.1)$ nm with a coincidence lattice of $(11.5 \pm 0.3) \times (11.5 \pm 0.3)$ with respect to the Au(111) surface ($a_{\text{Au}} = 0.289$ nm), in agreement with LEED. The EuAu$_2$ ML reveals a $(\sqrt{3} \times \sqrt{3})$R30° reconstruction on top of the Au(111) surface and a lattice parameter of 0.55 nm. a_m of EuAu$_2$ is 10% smaller than the one found in GdAu$_2$, HoAu$_2$, or YbAu$_2$, which have $a_m \approx 3.6$ nm [18,22].

B. Valency analysis by ResPES

The ResPES spectrum [see Fig. 1(b)] displays unequivocally the presence of a single Eu^{2+} multiplet peak and no further peaks related to Eu^{3+}, revealing the presence of only divalent Eu atoms exclusively located at the $EuAu_2$ ML. Eu atoms below the surface (either di- or trivalent) would give rise to an additional shifted multiplet [36] that does not appear in the spectra. Therefore, the existence of a single $EuAu_2$ ML with divalent character is probed.

C. Magnetic properties by XAS and XMCD

Figure 1(c) shows the XAS and XMCD spectra of an $EuAu_2$ ML at the Eu $M_{4,5}$ absorption edges ($T = 3$ K; $\mu_0 H = 6$ T and normal incidence). The XAS line shape confirms the divalent character of the Eu atom in $EuAu_2$ ML deduced from the ResPES spectra of Fig. 1(b) [see also the Supplemental Material (SM) [53], Fig. S4, for a comparison to the XAS spectrum of trivalent Eu_2O_3]. Magnetization curves in Fig. 1(d) are taken at different geometries and at the photon energy of the maximum M_5 XMCD peak while changing $\mu_0 H$. The out-of-plane magnetization curves with the field applied perpendicular to the surface saturates at approximately 2 T, while the in-plane magnetization curve reaches saturation at much higher applied fields, close to 6 T. This clearly reveals that the easy axis of magnetization is perpendicular to the plane. Magnetization loops were recorded at various temperatures, allowing an Arrott plot estimation [21,54] of the Curie temperature of the surface compound of $T_C = 13$ K [see the inset of Fig. 1(d)]. Further details are given in Fig. S5.

The OOP easy axis of magnetization in $EuAu_2$ MLs differs from the IP one of $GdAu_2$ [20,21], despite the identical $4f$ electronic configuration ($^8S_{7/2}$) and atomic structure. In the following, we explain this behavior in terms of their respective band structures measured by ARPES, which exhibits a clear dependence on the valence character of the REs, namely, divalent for Eu and trivalent for Gd. Further analysis by DFT provides insight into the spin-orbit effects on the individual bands.

D. Electronic structure by ARPES and DFT

Results of ARPES measurements performed on $EuAu_2$ MLs show the characteristic surface dispersive localized bands with Eu(d)-Au(s, p) character that are commonly found in all RAu$_2$ surface compounds [19,21,22] [see Figs. 2(d) and 2(e) and Figs. S1 and S2 in the SM]. Following the notation of Ref. [22], these valence bands are labeled A, B, C, and C'. As already seen in other RAu$_2$ materials, some of these bands are better detected in the first BZ, while other bands gain intensity in higher-order BZs. The $4f$ emissions of Eu are seen in the binding energy range between 1.1 and 0.4 eV, in agreement with ResPES in Fig. 1(b). To better visualize the valence band structure, a low photon energy of $h\nu = 21.2$ eV was chosen, where the $4f$ cross section is relatively low. Signs of hybridization between the localized Eu $4f$ level and the $EuAu_2$ valence bands are observed as kinks in the linear dispersion of the C bands in the second BZ and are marked with arrows in Fig. 2(e) (see also Fig. S2). Such $4f$-valence-band hybridizations have been observed for other Eu-based

bulks [55] and in $YbAu_2$ surface compounds [22]. The C band in $EuAu_2$ is characterized by a nearly conical shape at $\bar{\Gamma}$, with the apex above the Fermi level E_F. DFT band structure calculations for isolated and supported $EuAu_2$ MLs disclose the intersection above E_F of the C band (of d_{xy} character) with bands of $d_{x^2-y^2}$ and $d_{xz,yz}$ character, as shown in Fig. 2(c). These band crossings occur below (above) the Fermi energy for trivalent (divalent) RE ions [21,22]. Adding the 3 ML Au(111) substrate slab provides additional dispersive bands [21,22], which cause an upward shift of ≈ 0.1 eV in the $R(d)$-Au(s) hybrid band manifold, and a strong renormalization of $4f$ levels. Indeed, in the calculated freestanding $EuAu_2$ band structure the $4f$ states lie ≈ 0.7 eV lower. The $4f$ band of $EuAu_2$ is half filled, but as the individual bands are heavily split by hybridization with the A and C bands, it shows some degree of dispersion across the BZ. In contrast, the Gd($4f$) orbital in $GdAu_2$ barely interacts with the surrounding metal, showing a small crystal field splitting and no significant dispersion (see Fig. S3 in the SM).

E. Force theorem analysis

SOC at the crossings of the two-dimensional $R(d)$-Au(s) bands are sources of anisotropy that we characterize by DFT in the following. The SOC matrix element for two electrons belonging to orbitals of the same shell is

$$\langle lm\sigma | \xi_l \mathbf{l} \cdot \mathbf{s} | lm'\sigma' \rangle, \tag{1}$$

where $\mathbf{l}$ and $\mathbf{s}$ are the one-electron orbital and spin momentum operators; the l, m, and σ indices label the eigenstates of $\mathbf{l}$, l_z, and $\mathbf{s}$, respectively; and ξ_l is the SOC strength, which is approximately constant for all the electrons in each l shell. Intershell SOC is negligible. For hydrogenic atomic orbitals, these matrix elements are analytical and have been tabulated [56,57]. Selected combinations of m values and spin orientations give nonzero matrix elements. A second-order perturbative treatment of the SOC Hamiltonian term shows that this behavior is inherited by hybrid bands of an extended system [58–64]. In such a case, degeneracy lifting at band crossings obeys the rules imposed by the crystallographic symmetry of the system and the orbital symmetry of the bands for a given orientation of the spins.

In the so-called force theorem approach, where the SOC correction enters non-self-consistently in the DFT calculation, the MAE is obtained from the spin-orientation-dependent band energy contribution to the total energy of the system [45,47]:

$$\text{MAE} = \sum_{kn} \epsilon_{kn}^X f_{FD}\left(\epsilon_{kn}^X - E_F^X\right) - \sum_{kn} \epsilon_{kn}^Z f_{FD}\left(\epsilon_{kn}^Z - E_F^Z\right), \tag{2}$$

where the sum runs over the eigenenergies $\epsilon_{kn}^{\hat{s}_a}$ (k and n are the k-point and band indices, respectively), f_{FD} is the Fermi-Dirac function, and $E_F^{\hat{s}_a}$ are the Fermi energies for the spin orientations $\hat{s}_a = Z$ (out of plane) and X [the in-plane direction along the nearest RE atoms, shown in Fig. 2(a)]. The azimuthal dependence of the MAE is small. According to this equation, nonzero contributions to the MAE are generated at band crossings that become gapped for one spin orientation but not for the other. The final easy-axis direction
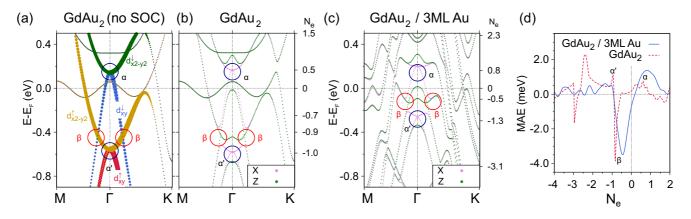
FIG. 3. Band structure and MAE of GdAu$_2$ as a function of band filling. (a) Orbital and spin characters of freestanding GdAu$_2$ bands in the absence of SOC. Band structure of (b) a freestanding and (c) supported GdAu$_2$ ML for spins aligned in the X (violet) and Z (green) directions in the force theorem approximation, with each calculation referred to its own Fermi level. The SOC-induced gaps at the band crossings relevant to the MAE are indicated with circles labeled α, α', and β. The right-hand axes show the corresponding band filling, i.e., the number of electrons N_e referred to charge neutrality. (d) MAE as a function of N_e for freestanding (solid line) and supported (dashed line) GdAu$_2$. Positive (negative) MAE values mean an OOP (IP) easy magnetization axis.

results from the integration of all individual gap contributions (with positive and negative small values) over occupied states. At crossings of fully occupied bands, the energy dispersion around the degeneracy point has to be asymmetrical in order to have a sizable contribution to MAE; otherwise, band energies around the gapped feature will cancel out each other. If the degeneracy lifting occurs exactly at the Fermi level, the contribution to the MAE will be large [47,65].

A spectral analysis of Eq. (2) is not possible, as the Fermi energy depends on the spin orientation. Instead, the common practice is to plot MAE vs N_e, i.e., MAE(N_e), where N_e is the number of electrons with respect to the neutral case ($N_e = 0$) calculated as an integral over the density of states of the system for each spin orientation; that is, each N_e value provides $E_F^{X,Z}(N_e)$ values [64–68]. Therefore, the MAE(N_e) curve allows us to assign a positive or negative MAE contribution to the region of the energy range close to $E_F^{X,Z}(N_e)$. As the Fermi energy fluctuation with the spin direction is small (a few meV), we use the $E_F(N_e)$ value calculated without SOC to guide the eye in the graphs. The value obtained at neutrality, MAE($N_e = 0$), corresponds to the expected anisotropy of the system. This type of MAE analysis relies on the validity of the force theorem approximation; namely, it assumes that there are only minor changes in the electron density (essentially, loss of collinearity) caused by the effect of SOC [46,47]. Despite the two RAu$_2$ compounds under study being heavy-atom systems, by comparing to fully self-consistent calculations of the band structures with SOC, we find that the force theorem properly accounts for the spin-orbit-induced gaps in an energy range of several eV around the Fermi energy (see Figs. S6 and S7 in the SM for GdAu$_2$ and EuAu$_2$, respectively).

1. GdAu$_2$

We apply this analysis to the band structure of freestanding and supported GdAu$_2$ MLs, as shown in Figs. 3(b) and 3(c). The band crossings labeled α and α' are degenerate for in-plane magnetization but are split by OOP magnetization. Figure 3(a) shows, as a guide for the eye, the orbital characters

and spin polarities in the absence of SOC for freestanding GdAu$_2$. The α and α' features are crossings between d_{xy} and $d_{x^2-y^2}$ ($m = \pm 2$) with *equal* spin polarization, a situation where the matrix element equation (1) foresees splitting by OOP magnetization. The Weyl nodal line β [69], which is a ring-shaped crossing around the Γ point between d_{xy} and $d_{x^2-y^2}$ bands with *opposite* spin polarization [see Fig. 3(a)], is split by in-plane magnetization according to Eq. (1).

Figure 3(d) shows the obtained MAE(N_e). The curves $E_F(N_e) - E_F(0)$ without SOC, shown in Fig. S9 in the SM, establish an approximate mapping between band fillings and binding energies [a few discrete values are given also on the right-hand axes in Figs. 3(b) and 3(c)]. For GdAu$_2$ close to neutrality ($N_e = 0$) the essential contributions to the MAE are those of the α, α', and β features. In the freestanding case, the β nodal ring results in the net sharp MAE peak of negative values in the dashed red line at $N_e = -0.9$ (i.e., contributing to the IP easy axis of magnetization), whereas features α and α' contribute to the OOP easy magnetization axis with peaks of positive MAE at $N_e = -1$ and just above $N_e = 0$ in the red dashed curve in Fig. 3(d). At neutrality we obtain an OOP easy axis with MAE(0) = 0.17 meV.

The same features, α, α', and β, appear for GdAu$_2$/3 ML Au(111), albeit at binding energies higher by ∼0.1 eV [see Figs. 3(b) and 3(c)], which also result in positive and negative contributions to the MAE around the neutrality point. The β line causes the in-plane peak at $N_e = -0.5$ (solid blue line), and α and α' contribute to the OOP magnetization easy axis with positive-valued MAE peaks at $N_e = -1.3$ and 0.8, respectively. At the neutrality point we find MAE(0) = -0.9 meV, i.e., an IP easy axis of magnetization, the same as observed experimentally. This is due to the contribution of the β gapped line, which dominates over the α and α' single-point gaps at Γ, aided by the fact that the β gapped line lies closer to E_F in the supported case. The contribution of the GdAu$_2$ $4f^7$ electrons to the anisotropy lies within the force theorem error since the departure from sphericity of this orbital is negligible when embedded in the alloy [in other words, the Gd($4f$) spin density cloud would be almost insensitive to the

applied field orientation, as shown in Fig. S3 in the SM]. Therefore, we attribute the experimental easy magnetization plane essentially to the MAE contribution of the dispersive Gd(d)-Au(s) bands.

2. EuAu$_2$

Next, we apply the force theorem methodology to the EuAu$_2$ bands. Bare inspection of the band structures of both freestanding and supported EuAu$_2$ MLs rules out the possibility of the anisotropy being dominated by the SOC effects on the Eu(d)-Au(s) hybrid bands for two reasons: (i) due to the divalent character of Eu, the d_{xy} and $d_{x^2-y^2}$ band crossings relevant for MAE are unoccupied [see Fig. 2(c)], and thus, they cannot contribute to the observed anisotropy, and (ii) the f band is heavily broadened by hybridization, with individual bands showing significant dispersion and spin orientation dependence [see Fig. S3(d) in the SM].

The force theorem equation (2) applied to the $U = 5.5$ eV band structures yields an OOP easy magnetization axis both for freestanding and supported EuAu$_2$, with MAE(0) = 1.0 and 1.54 meV, respectively [these are, respectively, the values taken by the red dashed and blue solid curves at neutrality in Fig. 4(a)]. The MAE peaks due to α', β, and α band crossing features are visible in the freestanding EuAu$_2$ bands above the charge neutrality level (see also Fig. S8). For EuAu$_2$/3 ML Au(111), Fig. 4(b) shows two large broad peaks at each MAE(N_e) curve, which take values $\simeq \pm 0.1$ eV at the electron filling ranges that correspond to the binding energy ranges where the hybridized $4f$ bands lie. The peak pairs account for the filling of the SOC-split band manifolds $4f_{7/2}$ and $4f_{5/2}$. In the calculation with $U = 5.5$ eV, these peaks occur at $N_e = -10$ and -5, respectively, corresponding to binding energies close to -1 eV [see also Figs. S9(b) and S9(c) in the SM]. These bands yield a non-negligible positive residual contribution to MAE(0) by virtue of the f-d hybridization. In a single-ion picture, this would be interpreted as a loss of sphericity of the half-filled $4f$ shell, which acquires a net nonzero $\langle L \rangle$ [9]. Figure S3 in the SM shows the magnetization distribution projected on $\hat{s}_a$ [$m_{\hat{s}_a}(\mathbf{r})$] of the Eu($4f$) shell embedded in the freestanding alloy monolayer, obtained by integration of the Kohn-Sham states in the binding energy range between -2.25 and -1.25 eV. The magnetization anisotropy distribution $m_X(\mathbf{r}) - m_Z(\mathbf{r})$ takes positive and negative values in plane and out of plane, respectively, which can be interpreted as the Eu(f) orbital spin density tendency to become deformed along the applied field direction. Note that the same quantity integrated for Gd(f) between -10 and -8.5 eV is an order of magnitude smaller.

The $4f$ contribution to the MAE of EuAu$_2$ can be further probed by modifying the U correlation parameter. We have carried out force theorem analyses for supported EuAu$_2$ with $U = 3.5$ and 7.5 eV. When U is decreased, the MAE energy is increased by $\simeq 1$ meV, and when U is increased, the easy axis of magnetization remains out of plane, but the MAE(0) value is reduced (see Fig. 4). The densities of states [Fig. S9(d) in the SM] show that a larger U value implies less hybridization between the $4f$ electrons and the hybrid bands of d character crossing the Fermi level. Indeed, for $U = 7.5$ eV the $4f$ band lies below $E_F - 1.5$ eV, i.e., close to the Au substrate states and below the d_{xy} band. For $U = 3.5$ eV, however, the $4f$
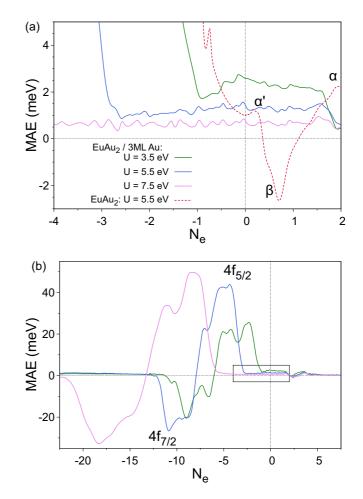

FIG. 4. MAE of EuAu$_2$ as a function of band filling. (a) MAE as a function of N_e for freestanding (solid blue line) and supported (dashed red line) EuAu$_2$ calculated with $U = 5.5$ eV close to the neutrality condition $N_e = 0$. Positive (negative) MAE values contribute to the OOP (IP) the IP easy axis. Additional solid curves show the results for EuAu$_2$/3 ML Au(111) with other U values. (b) Same curves in a wider range of N_e to show the large contributions of $4f$ electrons, switching the easy axis of magnetization from IP (negative MAE) to OOP (positive MAE). The rectangle corresponds to the close-up shown in (a).

band is centered at $E_F - 0.5$ eV, producing hybrid f-d states close to the Fermi level. This shows that the degree of f-d hybridization drives the MAE behavior of EuAu$_2$.

IV. CONCLUSIONS

To summarize, our XMCD experiments have determined that a EuAu$_2$ ML on Au(111) shows out-of-plane easy magnetization axis. Using photoemission experiments combined with DFT calculations, we showed that this is a consequence of the Eu^{2+} valence state and the f-d band hybridization. In contrast, the easy magnetization plane of GdAu$_2$ ML is explained by the Gd^{3+} valence and spin-orbit splitting of the point and line degeneracies of bands with d_{xy,x^2-y^2} character. The role of the RE valence is to determine whether these specific states are occupied or empty. This model of the contribution of the itinerant electrons to the magnetocrystalline anisotropy is a general result for the RAu$_2$ family of monolayer compounds. For R = Eu, Gd this is the only mechanisms

at work since the $4f$ orbital is half filled, i.e., $L = 0$. For RE atoms with nonzero L quantum numbers, there is a single-ion anisotropy that results from the interplay between spin-orbit and crystal field splittings of the $4f$ multiplet. For example, this multiplet mechanism dominates the OOP easy magnetization axis behavior in HoAu$_2$, where the valence is Ho^{3+} [22]. We predict the itinerant electrons yield MAE values of ≈ 1 meV in RAu$_2$ monolayers, irrespective of the L value. Therefore, the band and multiplet mechanisms may eventually compete.

ACKNOWLEDGMENTS

[1] K. H. J. Buschow and F. de Boer, *Physics of Magnetism and Magnetic Materials* (Kluwer Academic/Plenum, New York, 2003).

[2] R. Skomski and D. Sellmyer, Anisotropy of rare-earth magnets, J. Rare Earths **27**, 675 (2009).

[3] F. Donati, A. Singha, S. Stepanow, C. Wäckerlin, J. Dreiser, P. Gambardella, S. Rusponi, and H. Brune, Magnetism of Ho and Er Atoms on Close-Packed Metal Surfaces, Phys. Rev. Lett. **113**, 237201 (2014).

[4] F. Donati, S. Rusponi, S. Stepanow, C. Wäckerlin, A. Singha, L. Persichetti, R. Baltic, K. Diller, F. Patthey, E. Fernandes, J. Dreiser, Ž. Šljivančanin, K. Kummer, C. Nistor, P. Gambardella, and H. Brune, Magnetic remanence in single atoms, Science **352**, 318 (2016).

[5] A. Singha, R. Baltic, F. Donati, C. Wäckerlin, J. Dreiser, L. Persichetti, S. Stepanow, P. Gambardella, S. Rusponi, and H. Brune, $4f$ occupancy and magnetism of rare-earth atoms adsorbed on metal substrates, Phys. Rev. B **96**, 224418 (2017).

[6] F. D. Natterer, F. Donati, F. Patthey, and H. Brune, Thermal and Magnetic-Field Stability of Holmium Single-Atom Magnets, Phys. Rev. Lett. **121**, 027201 (2018).

[7] F. Donati, S. Rusponi, S. Stepanow, L. Persichetti, A. Singha, D. M. Juraschek, C. Wäckerlin, R. Baltic, M. Pivetta, K. Diller, C. Nistor, J. Dreiser, K. Kummer, E. Velez-Fort, N. A. Spaldin, H. Brune, and P. Gambardella, Unconventional Spin Relaxation Involving Localized Vibrational Modes in Ho Single-Atom Magnets, Phys. Rev. Lett. **124**, 077204 (2020).

[8] N. Ishikawa, M. Sugita, and W. Wernsdorfer, Quantum tunneling of magnetization in lanthanide single-molecule magnets: Bis(phthalocyaninato)terbium and bis(phthalocyaninato)dysprosium anions, Angew. Chem., Int. Ed. **44**, 2931 (2005).

[9] J. D. Rinehart and J. R. Long, Exploiting single-ion anisotropy in the design of f-element single-molecule magnets, Chem. Sci. **2**, 2078 (2011).

[10] M. J. Martínez-Pérez, S. Cardona-Serra, C. Schlegel, F. Moro, P. J. Alonso, H. Prima-García, J. M. Clemente-Juan, M. Evangelisti, A. Gaita-Ariño, J. Sesé, J. van Slageren, E. Coronado, and F. Luis, Gd-Based Single-Ion Magnets with Tunable Magnetic Anisotropy: Molecular Design of Spin Qubits, Phys. Rev. Lett. **108**, 247213 (2012).

[11] M. Mannini, F. Bertani, C. Tudisco, L. Malavolti, L. Poggini, K. Misztal, D. Menozzi, A. Motta, E. Otero, P. Ohresser, P. Sainctavit, G. G. Condorelli, E. Dalcanale, and R. Sessoli, Magnetic behaviour of TbPc$_2$ single-molecule magnets chemically grafted on silicon surface, Nat. Commun. **5**, 4582 (2014).

[12] B. W. Heinrich, L. Braun, J. I. Pascual, and K. J. Franke, Tuning the magnetic anisotropy of single molecules, Nano Lett. **15**, 4024 (2015).

[13] A. Chiesa, F. Cugini, R. Hussain, E. Macaluso, G. Allodi, E. Garlatti, M. Giansiracusa, C. A. P. Goodwin, F. Ortu, D. Reta, J. M. Skelton, T. Guidi, P. Santini, M. Solzi, R. De Renzi, D. P. Mills, N. F. Chilton, and S. Carretta, Understanding magnetic relaxation in single-ion magnets with high blocking temperature, Phys. Rev. B **101**, 174402 (2020).

[14] M. Briganti, E. Lucaccini, L. Chelazzi, S. Ciattini, L. Sorace, R. Sessoli, F. Totti, and M. Perfetti, Magnetic anisotropy trends along a full 4f-series: The f^{n+7} effect, J. Am. Chem. Soc. **143**, 8108 (2021).

[15] D. Givord, J. Laforest, H. S. Li, A. Liénard, R. Perrier de la Bâthie, and P. Tenaud, Rare earth-transition metal permanent magnets, J. Phys. Colloq. **46**, C6-213 (1985).

[16] K. Buschow, Intermetallic compounds of rare earths and nonmagnetic metals, Rep. Prog. Phys. **42**, 1373 (1979).

[17] M. Corso, M. J. Verstraete, F. Schiller, M. Ormaza, L. Fernández, T. Greber, M. Torrent, A. Rubio, and J. E. Ortega, Rare-Earth Surface Alloying: A New Phase for GdAu$_2$, Phys. Rev. Lett. **105**, 016101 (2010).

[18] M. Corso, L. Fernández, F. Schiller, and J. E. Ortega, Au(111)-based nanotemplates by Gd alloying, ACS Nano **4**, 1603 (2010).

[19] M. Ormaza, L. Fernández, S. Lafuente, M. Corso, F. Schiller, B. Xu, M. Diakhate, M. J. Verstraete, and J. E. Ortega, LaAu$_2$ and CeAu$_2$ surface intermetallic compounds grown by high-temperature deposition on Au(111), Phys. Rev. B **88**, 125405 (2013).

[20] L. Fernández, M. Blanco-Rey, M. Ilyn, L. Vitali, A. Magaña, A. Correa, P. Ohresser, J. E. Ortega, A. Ayuela, and F. Schiller, Co nanodot arrays grown on a GdAu$_2$ template: Substrate/nanodot antiferromagnetic coupling, Nano Lett. **14**, 2977 (2014).

[21] M. Ormaza, L. Fernández, M. Ilyn, A. Magaña, B. Xu, M. J. Verstraete, M. Gastaldo, M. A. Valbuena, P. Gargiani, A. Mugarza, A. Ayuela, L. Vitali, M. Blanco-Rey, F. Schiller, and

J. E. Ortega, High temperature ferromagnetism in a GdAg$_2$ monolayer, Nano Lett. **16**, 4230 (2016).

[22] L. Fernandez, M. Blanco-Rey, R. Castrillo-Bodero, M. Ilyn, K. Ali, E. Turco, M. Corso, M. Ormaza, P. Gargiani, M. A. Valbuena, A. Mugarza, P. Moras, P. M. Sheverdyaeva, A. K. Kundu, M. Jugovac, C. Laubschat, J. E. Ortega, and F. Schiller, Influence of 4f filling on electronic and magnetic properties of rare earth-Au surface compounds, Nanoscale **12**, 22258 (2020).

[23] N. D. Mermin and H. Wagner, Absence of Ferromagnetism or Antiferromagnetism in One- or Two-Dimensional Isotropic Heisenberg Models, Phys. Rev. Lett. **17**, 1133 (1966).

[24] V. L. Berezinskii, Destruction of long-range order in one-dimensional and two-dimensional systems having a continuous symmetry group I. Classical systems, Sov. Phys. JETP **32**, 493 (1971).

[25] J. M. Kosterlitz and D. J. Thouless, Ordering, metastability and phase transitions in two-dimensional systems, J. Phys. C **6**, 1181 (1973).

[26] D. J. W. Geldart, P. Hargraves, N. M. Fujiki, and R. A. Dunlap, Anisotropy of the Critical Magnetic Susceptibility of Gadolinium, Phys. Rev. Lett. **62**, 2728 (1989).

[27] M. Rotter, M. Loewenhaupt, M. Doerr, A. Lindbaum, H. Sassik, K. Ziebeck, and B. Beuneu, Dipole interaction and magnetic anisotropy in gadolinium compounds, Phys. Rev. B **68**, 144418 (2003).

[28] J. J. M. Franseand R. Gersdorf, Magnetic Anisotropy of Gd Metal at 4 K under Pressure, Phys. Rev. Lett. **45**, 50 (1980).

[29] M. Wietstruk, A. Melnikov, C. Stamm, T. Kachel, N. Pontius, M. Sultan, C. Gahl, M. Weinelt, H. A. Dürr, and U. Bovensiepen, Hot-Electron-Driven Enhancement of Spin-Lattice Coupling in Gd and Tb 4f Ferromagnets Observed by Femtosecond X-Ray Magnetic Circular Dichroism, Phys. Rev. Lett. **106**, 127401 (2011).

[30] M. Colarieti-Tosti, S. I. Simak, R. Ahuja, L. Nordström, O. Eriksson, D. Åberg, S. Edvardsson, and M. S. S. Brooks, Origin of Magnetic Anisotropy of Gd Metal, Phys. Rev. Lett. **91**, 157201 (2003).

[31] H. Jang, B. Y. Kang, B. K. Cho, M. Hashimoto, D. Lu, C. A. Burns, C.-C. Kao, and J.-S. Lee, Observation of Orbital Order in the Half-Filled 4f Gd Compound, Phys. Rev. Lett. **117**, 216404 (2016).

[32] F. Reinert, G. Nicolay, S. Schmidt, D. Ehm, and S. Hüfner, Direct measurements of the L-gap surface states on the (111) face of noble metals by photoelectron spectroscopy, Phys. Rev. B **63**, 115415 (2001).

[33] G. Nicolay, F. Reinert, S. Hüfner, and P. Blaha, Spin-orbit splitting of the L-gap surface state on Au(111) and Ag(111), Phys. Rev. B **65**, 033407 (2001).

[34] F. Gerken, J. Barth, and C. Kunz, Excited Multiplet Lines in Resonant Photoemission Spectra of Gd, Phys. Rev. Lett. **47**, 993 (1981).

[35] O.-P. Sairanen and S. Aksela, Resonance Auger and autoionization processes in solid gadolinium and europium following 4d to 4f resonant excitations with synchrotron radiation, J. Phys.: Condens. Matter **4**, 3337 (1992).

[36] W.-D. Schneider, C. Laubschat, and B. Reihl, Temperature-dependent microstructure of evaporated Yb surfaces, Phys. Rev. B **27**, 6538 (1983).

[37] G. Kaindl, A. Höhr, E. Weschke, S. Vandré, C. Schüßler-Langeheine, and C. Laubschat, Surface core-level shifts and

surface states for the heavy lanthanide metals, Phys. Rev. B **51**, 7920 (1995).

[38] H. Krakauer, M. Posternak, and A. J. Freeman, Linearized augmented plane-wave method for the electronic band structure of thin films, Phys. Rev. B **19**, 1706 (1979).

[39] E. Wimmer, H. Krakauer, M. Weinert, and A. J. Freeman, Full-potential self-consistent linearized-augmented-plane-wave method for calculating the electronic structure of molecules and surfaces: O$_2$ molecule, Phys. Rev. B **24**, 864 (1981).

[40] FLEUR, http://www.flapw.de.

[41] V. I. Anisimov, F. Aryasetiawan, and A. I. Lichtenstein, First-principles calculations of the electronic structure and spectra of strongly correlated systems: The LDA+U method, J. Phys.: Condens. Matter **9**, 767 (1997).

[42] A. B. Shick, A. I. Liechtenstein, and W. E. Pickett, Implementation of the LDA+U method using the full-potential linearized augmented plane-wave basis, Phys. Rev. B **60**, 10763 (1999).

[43] V. I. Anisimov, I. V. Solovyev, M. A. Korotin, M. T. Czyżyk, and G. A. Sawatzky, Density-functional theory and NiO photoemission spectra, Phys. Rev. B **48**, 16929 (1993).

[44] J. P. Perdew, K. Burke, and M. Ernzerhof, Generalized Gradient Approximation Made Simple, Phys. Rev. Lett. **77**, 3865 (1996).

[45] M. Weinert, R. E. Watson, and J. W. Davenport, Total-energy differences and eigenvalue sums, Phys. Rev. B **32**, 2115 (1985).

[46] C. Li, A. J. Freeman, H. J. F. Jansen, and C. L. Fu, Magnetic anisotropy in low-dimensional ferromagnetic systems: Fe monolayers on Ag(001), Au(001), and Pd(001) substrates, Phys. Rev. B **42**, 5433 (1990).

[47] G. H. O. Daalderop, P. J. Kelly, and M. F. H. Schuurmans, First-principles calculation of the magnetocrystalline anisotropy energy of iron, cobalt, and nickel, Phys. Rev. B **41**, 11919 (1990).

[48] D.-S. Wang, R. Wu, and A. J. Freeman, First-principles theory of surface magnetocrystalline anisotropy and the diatomic-pair model, Phys. Rev. B **47**, 14932 (1993).

[49] M. Methfessel and A. T. Paxton, High-precision sampling for Brillouin-zone integration in metals, Phys. Rev. B **40**, 3616 (1989).

[50] F. Gerken, Calculated photoemission spectra of the 4f states in the rare-earth metals, J. Phys. F **13**, 703 (1983).

[51] W. D. Schneider, C. Laubschat, G. Kalkowski, J. Haase, and A. Puschmann, Surface effects in Eu intermetallics: A resonant photoemission study, Phys. Rev. B **28**, 2017 (1983).

[52] Y. Que, Y. Zhuang, Z. Liu, C. Xu, B. Liu, K. Wang, S. Du, and X. Xiao, Two-dimensional rare earth–gold intermetallic compounds on Au(111) by surface alloying, J. Phys. Chem. Lett. **11**, 4107 (2020).

[53] See Supplemental Material at http://link.aps.org/supplemental/10.1103/PhysRevResearch.4.013237, which includes additional Refs. [70–72], further details on the XMCD and ARPES experiments and DFT calculations.

[54] A. Arrott, Criterion for ferromagnetism from observations of magnetic isotherms, Phys. Rev. **108**, 1394 (1957).

[55] S. Danzenbächer, D. V. Vyalikh, Y. Kucherenko, A. Kade, C. Laubschat, N. Caroca-Canales, C. Krellner, C. Geibel, A. V. Fedorov, D. S. Dessau, R. Follath, W. Eberhardt, and S. L. Molodtsov, Hybridization Phenomena in Nearly-Half-Filled f-Shell Electron Systems: Photoemission Study of EuNi$_2$P$_2$, Phys. Rev. Lett. **102**, 026403 (2009).

[56] E. Abate and M. Asdente, Tight-binding calculation of 3d bands

of Fe with and without spin-orbit coupling, Phys. Rev. **140**, A1303 (1965).

[57] C. Elsasser, M. Fahnle, E. H. Brandt, and M. C. Bohm, Theory of local magnetic anisotropy in amorphous alloys, J. Phys. F **18**, 2463 (1988).

[58] H. Takayama, K.-P. Bohnen, and P. Fulde, Magnetic surface anisotropy of transition metals, Phys. Rev. B **14**, 2287 (1976).

[59] P. Bruno, Tight-binding approach to the orbital magnetic moment and magnetocrystalline anisotropy of transition-metal monolayers, Phys. Rev. B **39**, 865 (1989).

[60] M. Cinal, D. M. Edwards, and J. Mathon, Magnetocrystalline anisotropy in ferromagnetic films, Phys. Rev. B **50**, 3754 (1994).

[61] G. van der Laan, Microscopic origin of magnetocrystalline anisotropy in transition metal thin films, J. Phys.: Condens. Matter **10**, 3239 (1998).

[62] L. Ke and M. van Schilfgaarde, Band-filling effect on magnetic anisotropy using a Green's function method, Phys. Rev. B **92**, 014423 (2015).

[63] O. Šipr, S. Mankovsky, S. Polesya, S. Bornemann, J. Minár, and H. Ebert, Illustrative view on the magnetocrystalline anisotropy of adatoms and monolayers, Phys. Rev. B **93**, 174409 (2016).

[64] M. Blanco-Rey, J. I. Cerdá, and A. Arnau, Validity of perturbative methods to treat the spin–orbit interaction: Application to magnetocrystalline anisotropy, New J. Phys. **21**, 073054 (2019).

[65] G. H. O. Daalderop, P. J. Kelly, and M. F. H. Schuurmans, Magnetic anisotropy of a free-standing Co monolayer and of multilayers which contain Co monolayers, Phys. Rev. B **50**, 9989 (1994).

[66] T. Moos, W. Hübner, and K. Bennemann, Magnetocrystalline anisotropy energy of a transition metal monolayer: A nonperturbative theory, Solid State Commun. **98**, 639 (1996).

[67] A. Lessard, T. H. Moos, and W. Hübner, Magnetocrystalline anisotropy energy of transition-metal thin films: A nonperturbative theory, Phys. Rev. B **56**, 2594 (1997).

[68] P. Ravindran, A. Kjekshus, H. Fjellvåg, P. James, L. Nordström, B. Johansson, and O. Eriksson, Large magnetocrystalline anisotropy in bilayer transition metal phases from first-principles full-potential calculations, Phys. Rev. B **63**, 144409 (2001).

[69] B. Feng, R.-W. Zhang, Y. Feng, B. Fu, S. Wu, K. Miyamoto, S. He, L. Chen, K. Wu, K. Shimada, T. Okuda, and Y. Yao, Discovery of Weyl Nodal Lines in a Single-Layer Ferromagnet, Phys. Rev. Lett. **123**, 116401 (2019).

[70] B. T. Thole, G. van der Laan, J. C. Fuggle, G. A. Sawatzky, R. C. Karnatak, and J.-M. Esteva, $3d$ x-ray-absorption lines and the $3d^9 4f^{n+1}$ multiplets of the lanthanides, Phys. Rev. B **32**, 5107 (1985).

[71] T. Kinoshita, H. Gunasekara, Y. Takata, S.-I. Kimura, M. Okuno, Y. Haruyama, N. Kosugi, K. Nath, H. Wada, A. Mitsuda, M. Shiga, T. Okuda, A. Harasawa, H. Ogasawara, and A. Kotani, Spectroscopy studies of temperature-induced valence transition on $EuNi_2(Si_{1-x}Ge_x)_2$ around Eu 3d–4f, 4d–4f and Ni 2p–3d excitation regions, J. Phys. Soc. Jpn. **71**, 148 (2002).

[72] A. Tcakaev, V. B. Zabolotnyy, C. I. Fornari, P. Rüßmann, T. R. F. Peixoto, F. Stier, M. Dettbarn, P. Kagerer, E. Weschke, E. Schierle, P. Bencok, P. H. O. Rappl, E. Abramof, H. Bentmann, E. Goering, F. Reinert, and V. Hinkov, Incipient antiferromagnetism in the Eu-doped topological insulator Bi_2Te_3, Phys. Rev. B **102**, 184401 (2020).